Magnetic resonance characterization of coupled gas and particle dynamics in a bubbling fluidized bed

C. M. Boyce,[1,2,*] N. P. Rice,[1] A. Ozel,[2] J. F. Davidson,[1] A. J. Sederman,[1] L. F. Gladden,[1] S. Sundaresan,[2] J. S. Dennis,[1] and D. J. Holland[1,3]

[1]*Department of Chemical Engineering and Biotechnology, University of Cambridge, Cambridge CB2 3RA, United Kingdom*

[2]*Department of Chemical and Biological Engineering, Princeton University, Princeton, New Jersey 08544, USA*

[3]*Department of Chemical and Process Engineering, University of Canterbury, Christchurch, New Zealand*

(Received 22 March 2016; published 2 November 2016)

Relative flow between granular material and gas can create phenomena in which particles behave like a liquid with bubbles rising through them. In this paper, magnetic resonance imaging is used to measure the velocities of the gas and solid phases in a bubbling fluidized bed. Comparison with theory shows that the average velocity of gas through the interstices between particles is predicted correctly by classic analytical theory. Experiments were also used to validate predictions from computer simulations of gas and solid motion. The experiments show a wide distribution of gas velocities in both bubbling and emulsion regions, providing a different direction for computational and analytical theory.

DOI: 10.1103/PhysRevFluids.1.074201

I. INTRODUCTION

Granular material displays solidlike, liquidlike, and gaslike properties, creating complicated flow patterns, which present formidable challenges in characterization [1–3] in part because conventional techniques cannot measure particle and gas dynamics quantitatively in opaque, three-dimensional systems. Examples in which granular matter displays liquidlike properties include desert-dwelling animals "swimming" through sand [4], liquefaction during earthquakes [5], "bubbles" of gas rising through assemblies of solid particles [6], and an effective "surface tension" in granular streams falling through air [7]. Although conveying of granular materials is used widely in industry, understanding these flows presents challenges, giving uncertainty in plant design and potentially reduced output from industrial processes [8]. This difficulty in understanding systems employing granular flow stems from challenges in characterizing them experimentally, especially two-phase systems employing gas and particles.

Fluidized beds are an important example of gas-particle flows, exhibiting fascinating phenomena such as bubbling; they are used in key processes in the chemicals, energy, food, and pharmaceutical industries. A fluidized bed can be formed in a vertical cylinder containing granular particles through which gas flows upward. At a critical gas velocity, the minimum fluidization velocity U_{mf}, the drag force on the particles balances the gravitational force; the particles then exhibit liquidlike behavior [6]. At velocities above U_{mf}, bubbles of gas may rise through the system, causing rapid mixing and efficient contact between the gas and particles. Such contact is needed in, e.g., systems where the gas and solids have to react chemically while maintaining a nearly uniform temperature distribution. Analytical theory [6,9] and computer simulations [10] capture key elements of these macroscale hydrodynamics and indicate that fluidized beds can be highly selective and minimize waste, making them ideal for the development of green processes [11]. However, a lack of detailed, quantitative measurements of gas motion and mesoscale dynamics has limited the introduction of these processes at the industrial scale [12]. In this paper we report spatially resolved magnetic

*Corresponding author: cmboyce@princeton.edu

TABLE I. Fluidized bed properties.

Bed property	Value
inner diameter D_{bed}	52 mm
tapped bed height H_0	100 mm
particle type	poppy seeds
particle diameter d_p	1.1 mm
Geldart [27] grouping	D
U_{mf}	0.090 ± 0.002 m/s
U_{mb}	0.090 ± 0.002 m/s
gas molecule	SF_6
pressure	8.5 bar
temperature	25 ± 3 °C
gas density ρ	56 kg/m^3
gas viscosity μ	1.610^{-5} Pa s
distributor type	porous bronze plate

resonance imaging (MRI) measurements of gas velocity distributions within a fluidized bed and use the results to interrogate the analytical theory of two-phase fluidization and commonly used Euler-Lagrange simulations of fluid-particle flows.

Various techniques are available to measure granular dynamics [13–15] and liquid flow [16,17]. Measurements on gases are possible in dilute granular flow [18] and MRI has been used to map flows of gas in fixed beds of solids [19]. However, the high diffusivity and low density of gases makes measurements challenging, especially when coupled with rapid motion of particles. Fluidized beds use particles with diameters d_p of $\sim$1 mm or less; previous MRI techniques have not been able to measure gas velocity accurately in beds of particles so small. Differences in the magnetic susceptibility between particles and fluid cause local variations in the strength of the magnetic field; these variations affect the measurement of motion. For low velocities of gas ($<$0.05 m/s), the field variations are overcome by using appropriate radio-frequency pulses to reverse the effect of the unwanted local variations in the magnetic field [20]. However, such an approach breaks down when studying faster flows of gas passing through beds of finer particles, e.g., in a fluidized bed, where local variations in the magnetic field are not constant for the required duration between radiofrequency pulses ($\sim$1 ms) and hence measurements are not quantitative [21,22].

The only previous characterization of gas flow in fluidized beds using magnetic resonance used spatially unresolved NMR to measure gas exchange coefficients between bubble, emulsion, and absorbed states [23–26]. One of these studies [24] also conducted one-dimensional MRI measurements on particles to determine bubble rise velocities. Two of these studies [23,26] conducted preliminary, spatially unresolved measurements of gas velocity distribution, showing wider distributions in gas velocities with increasing flow rate. In this study we demonstrate the quantitative accuracy of our measurements and resolve gas velocity distributions spatially to view flow behavior in bubbling and emulsion regions.

II. MATERIALS AND METHODS

A. Fluidized bed arrangement

Gas velocity measurements were conducted in a fluidized bed of particles contained in a PVC pipe. Details of the fluidized bed are summarized in Table I. The bed had an internal diameter $D_{\text{bed}} = 52$ mm and was filled with poppy seeds of diameter $d_p = 1.1$ mm to a tapped bed height $H_0 = 100$ mm. The bed was fluidized using sulfur hexafluoride (SF_6) gas at a pressure of 8.5 bar. The gas was kept at 8.5 bar in the bed in order to increase the NMR signal from it, as well as increase its relaxation times. Sulfur hexafluoride was chosen because each molecule contains six fluorine nuclei

TABLE II. Relaxation times.

Molecule	T_1 (ms)	T_2 (ms)	T_2^* (ms)
SF_6 in freeboard	20	13	0.5
SF_6 in bed of particles	19	10	0.2
oil in poppy seeds	373	75	0.3

and therefore the NMR signal is strong. In addition, the diffusivity of sulfur hexafluoride is low for a gas, which increases the resolution that can be achieved. Sulfur hexafluoride also has a relatively short T_1 relaxation time (20 ms at 8.5 bars), which permits a fast repetition rate for the experiments and hence reduces the total duration of the experiments. With the temperature of the SF_6 controlled at 25 ± 3 °C, its density was 56 kg/m^3 and its viscosity was approximately 1.6×10^{-5} Pa s. The particles were group D according to Geldart's [27] classification. The minimum fluidization velocity U_{mf}, which is the superficial, or open pipe, gas velocity at minimum fluidization, was measured to be 0.090 ± 0.002 m/s based on the differential pressure across the bed. MRI was used to observe the onset of bubbling at $U_{mb} = 0.090 \pm 0.002$ m/s. The values of U_{mf} and U_{mb} were thus found to be equal; this is to be expected for particles of group B or D. A porous plate distributor approximately 50 mm in diameter made of 250 μm of sintered bronze was used. The plenum chamber beneath the distributor was filled with glass beads 2 mm in diameter. The pressure drop across the distributor was approximately 10 mbar at minimum fluidization, which is greater than the 6-mbar pressure drop across the bed, thus ensuring even fluidization. MRI measurements of gas velocity near the distributor were indicative of an even distribution of gas.

B. MRI arrangement

MRI measurements were conducted using a Bruker DMX 200 spectrometer with a magnetic field strength of 4.7 T. The magnet was operated at a proton (^{1}H) frequency of 199.7 MHz to measure signal from the oil in the poppy seeds and a ^{19}F frequency of 187.9 MHz to measure signal from the SF_6 gas. This separation of frequencies allowed the signal from the particles and gas to be measured separately without interference. A birdcage radio-frequency (rf) coil (capable of tuning to either the ^{1}H or the ^{19}F frequency) with an inner diameter of 64 mm was situated around the fluidized bed to excite and detect signal from the seeds and gas. A shielded three-axis gradient set capable of producing a maximum gradient of 0.139 T/m was used for imaging and velocimetry purposes.

The relaxation times (T_1, T_2, and T_2^*) for the poppy seeds and SF_6 gas were measured to determine repetition times for successive MRI scans. These times are shown in Table II. The repetition times were chosen as 3–5 times the spin-lattice relaxation time T_1 so as to allow the net magnetization to return almost completely to the vertical (z) axis before the next excitation. The apparent transverse relaxation time T_2^* for both gas and particles was short, owing to background gradients arising from the difference in the magnetic susceptibility of the particles and the gas.

C. Horizontally averaged measurements of time-averaged gas velocity

Measurements of gas velocity averaged over the cross section of the fluidized bed were conducted in the bed of particles under packed bed conditions in order to determine whether the gas velocity was measured accurately in a densely packed bed of small particles. The established 13-interval [20] pulse sequence was used as a control, representing the current state of the art, and compared with the recently developed 11-interval pulse sequence [28]. Figure 1 shows a diagram of the rf pulses as well as the slice G_{slice} and flow-encoding g_{flow} gradients used for this pulse sequence. As detailed elsewhere [28], the pulse sequence was based on the 13-interval pulse sequence but designed to minimize the echo time τ and hence reduce the effect of the inhomogeneous magnetic field arising from the different magnetic susceptibility of the gas and particles. The inhomogeneous magnetic

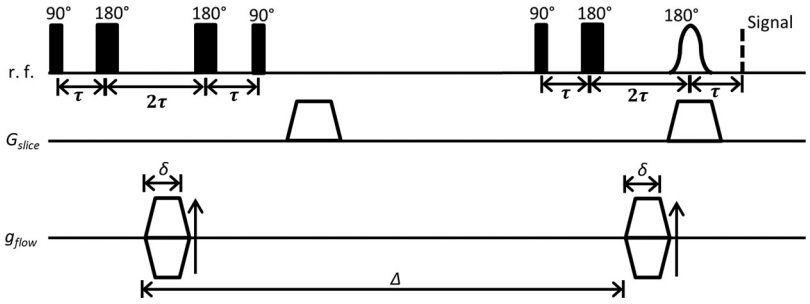

FIG. 1. Pulse sequence diagram for 11-interval MRI velocimetry.

field was found to selectively attenuate signal from fast moving nuclei at high ($>0.03\,\mathrm{ms}^{-1}$) gas velocities [28]. The attenuation occurs while the magnetization is in the transverse plane (i.e., during the echo time). Thus the reduction in the echo time permitted by the 11-interval pulse sequence led to its increased accuracy in the measurement of the gas velocity. The parameters for the gas velocity measurements of the two pulse sequences are given in Table III. For the 13- and 11-interval pulse sequences, the echo times τ and flow-encoding times δ were as short as possible given the slew rate limits for the gradient systems for the MRI system used. The observation times Δ were 6 ms, which is sufficiently long to encode for coherent motion, but short enough to avoid issues with fast moving signal leaving the rf coil undetected.

The range of velocities measured by MRI is determined by the field of flow, which is a function of the gradient strength, and timing parameters of the pulse sequence. For all experiments reported, the field of flow was kept constant at 2 m/s. The maximum gradient strength used for the experiments g_{flow} was 0.139 T/m.

To assess the accuracy of the measurements, the expected gas velocity $u_{z,\mathrm{expected}}$ was evaluated according to

$$u_{z,\mathrm{expected}}\,(U) = \frac{U}{1-\phi(U)}, \tag{1}$$

where $\phi(U)$ is the solid volume fraction at a given superficial velocity and is defined by the void fraction ε according to $\phi = 1-\varepsilon$, and U is defined as the volumetric flow rate divided by the cross-sectional area of the bed. The packing fraction was evaluated using magnetic resonance

TABLE III. Parameters for cross-section-averaged measurements of vertical gas velocity with different pulse sequences.

Parameter	13 intervals	11 intervals
field of flow	2.00 m/s	2.00 m/s
FWHM slice thickness z	4 mm	4 mm
phase cycling	8-step cogwheel	12-step cogwheel
observation time Δ	6 ms	6 ms
flow-encoding gradient period δ	100 μs	100 μs
echo time τ	780 μs	360 μs
recycle time	75 ms	75 ms
number of averages	3	2
acquisition time	30 s	30 s

TABLE IV. Parameters for measurements of maps of gas velocity.

Parameter	Value
field of view $x \times y$	$60 \times 60\,\text{mm}^2$
FWHM slice thickness z	4 mm
resolution $x \times y$	$3.75 \times 3.75\,\text{mm}^2$
pixel size $x \times y$	$0.47 \times 0.47\,\text{mm}^2$
pulse sequence	11 intervals
phase cycling	12-step cogwheel
observation time Δ	6 ms
flow-encoding gradient period δ	100 μs
echo time τ	360 μs
field of flow	3 m/s
recycle time T_R	75 ms
number of flow-encoding gradients	3
number of averages N_{avg}	8
acquisition time	80 min

measurements of the poppy seeds, according to

$$\phi(U) = \phi_{\text{packed}} \frac{S(U)}{S_{\text{packed}}}, \tag{2}$$

where $S(U)$ is the signal from a slice-selective spin echo pulse sequence on the poppy seeds at a given superficial velocity U and S_{packed} is the corresponding signal with the bed under packed conditions, for which the solids volume fraction was $\phi_{\text{packed}} = 0.57$. The low value of ϕ_{packed} was due to the nonsphericity of the particles. This value of ϕ_{packed} was measured by filling a graduated cylinder to a specified volume V_{packed} with poppy seeds. The packed volume V_{packed} consists of the volume of the seeds and the interstitial gas. The volume of the poppy seeds alone V_{seeds} was determined by submerging the seeds underwater in a graduated cylinder and measuring the increase volume after adding the seeds. Knowing the packed volume of the seeds V_{packed} and the actual volume of the seeds V_{seeds}, the packing fraction was

$$\phi_{\text{packed}} = \frac{V_{\text{seeds}}}{V_{\text{packed}}}. \tag{3}$$

D. Maps of time-averaged velocity and void fraction

Maps of gas velocity were acquired in the bed of particles using the 11-interval pulse sequence shown in Fig. 1, but with additional phase-encoding gradients used for imaging. The phase-encoding gradients were applied at the same time as the second flow-encoding gradient. Parameters for these measurements are summarized in Table IV. The experimental determinations of gas velocity were obtained using a circular sampling of 193 points on a 16×16 Cartesian grid in k space. The circular sampling was used to decrease the acquisition times (256 points would need to be acquired for a full image in k space) without losing significant signal intensity or sharpness of the circular image in real space. For images in the bed of particles, eight averages were acquired requiring a total time of approximately 80 min. Images were zero filled to 128×128 Cartesian grid points prior to Fourier transformation. The maximum spatial frequency measured was $\sim 150\,\text{m}^{-1}$, corresponding to a resolution of 3.75 mm. Throughout this paper, the phrase pixel size is used to define the dimensions of pixels in the images after zero filling, which in all cases was 0.47 mm; the resolution is determined by the maximum spatial frequency measured. A 12-step cogwheel phase cycle was used, determined with the CCCP++ software [29], to negate erroneous signal arising in individual, free-induction decay readings. MRI measurements were made under bubbling fluidization conditions

TABLE V. Parameters for the acquisition of maps of particle velocity and void fraction.

Parameter	Value
field of view $x \times y$	$60 \times 60\,\text{mm}^2$
FWHM slice thickness z	4 mm
resolution $x \times y$	$3.75 \times 3.75\,\text{mm}^2$
pixel size $x \times y$	$0.47 \times 0.47\,\text{mm}^2$
pulse sequence	spin echo
phase cycling	4 steps
observation time Δ	2.33 ms
flow-encoding gradient period δ	100 μs
echo time τ	2 ms
field of flow	3 m/s
recycle time T_R	1.12 s
number of flow-encoding gradients	3
number of averages N_{avg}	4
acquisition time	180 min

with $U = 0.104\,\text{m/s}$ and in a packed bed state ($U < U_{mf}$, i.e., the particles were stationary) with $U = 0.080$ and 0.065 m/s. These measurements were made at a variety heights in the bed. The expanded bed height for $U = 0.104\,\text{m/s}$ was $H = 120\,\text{mm}$. Determinations of gas velocity were made only for its vertical (z) component; images attempted for the horizontal components of the gas velocity showed interference with the imaging gradients, hence quantitative maps of velocity in the x and y directions were unobtainable.

Maps of particle velocities were also determined, at various heights above the distributor, using a spin echo pulse sequence [30] with the parameters in Table V. The parameters in Table V were such that the pixel size was the same as for the maps of gas velocity; thus, particle and gas velocities could be compared directly. For the particles, circular sampling was used with four averages in k space and a four-step phase cycle. The recycle time for the particle measurements was 1.12 s, thus exceeding the T_1 of the oil in the particles, 373 ms; hence, the total acquisition time was approximately 180 min. The images were reconstructed by zero filling to 128×128 grid points, prior to Fourier transformation. Intensity maps were approximately piecewise constant and therefore these were reconstructed to 128×128 pixels using a compressed sensing algorithm to minimize Gibbs ringing artifacts [31]. From the k-space maps in which no flow gradient was turned on, maps of signal intensities arising from the particles were acquired and converted into maps of void fraction. For this conversion, an intensity map was first acquired of a packed bed with a solids volume fraction of $\phi = 0.57$. The signal for each pixel is dependent on the sensitivity of the radio-frequency coil. These variations also occur in images under flow conditions; hence, for images in the fluidized bed, the solid volume fraction for each pixel was assessed using the ratio of the signal intensity to the signal intensity from the corresponding packed bed image:

$$\phi_{\text{fluidized}}(x,y) = \phi_{\text{packed}} \frac{S_{\text{fluidized}}(x,y)}{S_{\text{packed}}(x,y)}. \tag{4}$$

Here $\phi_{\text{fluidized}}(x,y)$ is the solid volume fraction of the pixel at coordinates x and y in a map under fluidized conditions, ϕ_{packed} is the solid volume fraction for a packed bed (volumetrically measured to be 0.57), $S_{\text{packed}}(x,y)$ is the signal intensity from a pixel in the packed bed map, and $S_{\text{fluidized}}(x,y)$ is the signal intensity from the corresponding pixel in the fluidized map. The maps of packing fraction for the fluidized images were then converted into void fraction maps using

$$\varepsilon_{\text{fluidized}}(x,y) = 1 - \phi_{\text{fluidized}}(x,y), \tag{5}$$

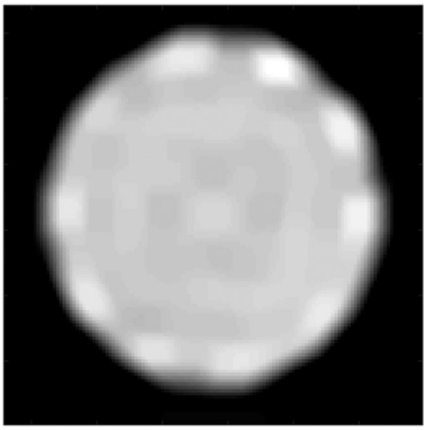

FIG. 2. Map of signal intensity arising from oil in poppy seeds in a packed bed used to calibrate the void fraction in fluidized bed measurements with white regions indicating high signal intensity and black regions indicating zero signal. The field of view $x \times y$ is $60 \times 60\,\mathrm{mm}^2$, the slice thickness is 4 mm, $z = 50$ mm above the distributor, and the pixel size $x \times y$ is $0.47 \times 0.47\,\mathrm{mm}^2$.

where $\varepsilon_{\mathrm{fluidized}}(x,y)$ is the void fraction at a pixel of a fluidized map. Figure 2 shows the map of signal intensity of a packed bed used in Eq. (4). Figure 2 shows variations in intensity due to sensitivity of the radio-frequency coil; additional variations in intensity owing to partial volume effects and Gibbs ringing can be seen around the perimeter of the image. These effects are largely negated in the voidage maps under flow conditions by using the calculation shown in Eq. (4).

For comparison of flow patterns between simulation predictions and experimental results and assessment of the accuracy of measurements, it was useful to quantify average gas velocities in maps or regions of maps. The average velocity $u_{z,\mathrm{avg}}$ was calculated by weighting the gas velocity by the void fraction on a pixel-by-pixel basis:

$$u_{z,\mathrm{avg,map}} = \frac{\sum_{N_{\mathrm{pixels}}} u_z(x,y)\varepsilon(x,y)}{\sum_{N_{\mathrm{pixels}}} \varepsilon(x,y)}, \tag{6}$$

where N_{pixels} is the number of pixels in the averaging region and $u_z(x,y)$ and $\varepsilon(x,y)$ are the measured time-averaged vertical gas velocity and void fraction in a pixel of the averaging region, respectively.

E. Measurements of distributions of gas velocities

Measurements of velocity distributions of SF_6 gas averaged across the horizontal cross section of the bed were acquired at different superficial velocities using propagator measurements. Propagator measurements are an MRI technique similar to velocity measurements, but they use a number of small increments in the magnitude of the flow-encoding gradient to determine a distribution of velocities rather than an average velocity. The parameters for these propagator measurements in the bed of particles and the freeboard are summarized in Table VI. For all propagator measurements, the 11-interval pulse sequence [28] was used. The observation time Δ was increased to 15 ms to enable 16 gradient steps to be acquired with a field of flow of 2 m/s. Longer observation times were not used as the signal-to-noise ratio became too low beyond this value and the signal from fast moving gas could have been missed due to the limited size of the rf coil. The measurements were conducted to determine the distribution of the vertical component of gas velocity at a position $z = 50$ mm above the distributor.

TABLE VI. Parameters for measurements of gas velocity distributions averaged over the cross section of the bed.

Parameter	Value
field of flow	2.00 m/s
FWHM slice thickness z	4 mm
velocity resolution	0.0625 m/s
pulse sequence	11 intervals
phase cycling	12-step cogwheel
observation time Δ	15 ms
flow-encoding gradient period δ	100 μs
echo time τ	360 μs
recycle time T_R	75 ms
number of flow-encoding gradients	16
number of averages N_{avg}	128
acquisition time	65 min

Average velocities from the velocity distributions were calculated using

$$u_{z,\text{avg,distribution}} = \frac{\sum_{i=1}^{N_{\text{vel}}} u_{z,i} S_i}{\sum_{i=1}^{N_{\text{vel}}} S_i}. \tag{7}$$

Here $u_{z,i}$ is the value of velocity for bin i, N_{vel} is the number of velocity bins in the distribution, and S_i is the signal from bin i.

F. Map of the distribution of gas velocities at each cross-sectional position

A cross-sectional map of the distribution of vertical gas velocities was acquired for the bubbling fluidization case $U = 0.104\,\text{m/s}$, at a position $z = 50\,\text{mm}$ above the distributor. This map was acquired in order to understand gas flow patterns in the bubbling and emulsion regions of a bubbling fluidized bed. The imaging parameters used for the measurement were the same as in the maps of gas velocity, shown in Table V. The velocity distribution parameters were the same as in the unresolved propagator measurements in the z direction, shown in Table VI. The number of averages was reduced to 4 so as to avoid a prohibitively long acquisition time. The acquisition time was still long, 6.5 h, and thus measurements were not conducted at other superficial velocities or positions in the bed.

G. Computer simulations

Computational fluid dynamics–discrete element method (CFD-DEM) simulations were run using open-source CFDEM [32] software that couples the DEM capabilities of LIGGGHTS [33] with the CFD capabilities of OPENFOAM [34]. Simulation parameters were set to match the system exactly, except that, for DEM purposes, spherical particles were simulated, even though the actual particles had a kidney shape.

The DEM was used to model the motion of each individual particle using contact mechanics and Newtonian physics. The DEM parameters are summarized in Table VII. A Hertzian spring model was used for normal and tangential contacts with a coefficient of restitution set to 0.93. This value of the coefficient of restitution was chosen to match that used in previous CFD-DEM studies using poppy seeds [35–38]; a CFD-DEM study that varied the coefficient of restitution from 0.47 to 0.97 and compared predictions with measurements of poppy seed velocity found the effect of coefficient of restitution to be minimal [39]. Coulomb's law was used to account for sliding, with a coefficient of friction for particle-particle interactions of 0.4 used based on the experimental value [40]. The

TABLE VII. Discrete element model parameters used in CFD-DEM simulations.

Parameter	Value
tapped bed height H_0	100 mm
bed diameter D_{bed}	52 mm
particle shape	spherical
particle diameter d_p	1.07 mm
particle density	1040 kg/m^3
coefficient of restitution	0.93
coefficient of friction (particle-particle)	0.4
coefficient of friction (particle-wall)	0.8
Young's modulus	1.2 MPa
spring model	Hertzian

coefficient of friction for particle-wall interactions was unknown, but was varied and found to have a negligible impact on simulation predictions.

Computational fluid dynamics was used to model the gas phase as a continuum, with a discretized form of the volume-averaged fluid equations [41] used to solve for gas velocity and pressure on a colocated fluid grid. The CFD parameters used are summarized in Table VIII. A code for incompressible flow was used with an implicit solver to allow for longer time steps. An unstructured grid was used to fit the cylindrical shape of the bed with mostly rectangular cells used in the center of the system and wedge-shaped cells used near the walls. The grid spacing in the vertical direction was $dz = 4$ mm, between 3 and 4 particle diameters, in order to achieve grid independent results while satisfying the conditions for the volume-averaged fluid equations [35,42]. Similar grid spacing was used in the horizontal direction.

At the inlet, the gas velocity was set to match the superficial velocity used in experiments, with an even distribution of gas to match the expected distribution obtained from the porous plate used experimentally. The diameter of the inlet area was set to 40 mm, to match the diameter of the plenum chamber. At the outlet, a constant pressure boundary condition was used. The no-slip boundary condition was used along the walls. Gas and particle motion were linked using the drag law of Beetstra *et al.* [43].

The particles in the experiments were nonspherical. In an effort to model the nonsphericity of the experimental particles, "effective particle diameters" were used in the model. In this approach, the particles were modeled as spherical in all aspects of the simulations, but different particle diameters

TABLE VIII. Computational fluid dynamics parameters used in CFD-DEM simulations.

Parameter	Value
overall height of simulation	400 mm
bed diameter D_{bed}	52 mm
fluid grid spacing	~4 mm
number of fluid grids	145 000
superficial velocity U	0.104 m/s
inlet gas diameter	40 mm
wall boundary condition	no slip
outlet boundary condition	constant pressure
gas density	52 kg/m^3

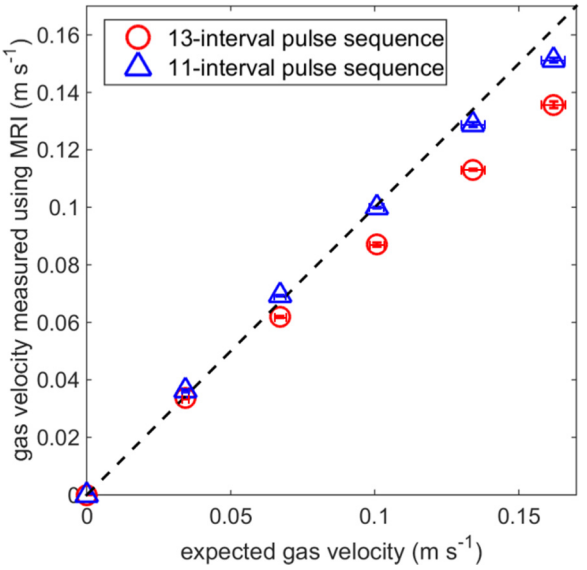

FIG. 3. Measurements of the vertical component of SF_6 gas velocity through a packed bed (i.e., no fluidization) of poppy seeds ($d_p = 1.1$ mm). The measurements give the average gas velocity over the cross section of the bed at a height 50 mm above the distributor. Measurements were made using (○) the Cotts 13-interval pulse sequence [20], which is widely regarded as the best existing MRI technique for measuring flow in heterogeneous systems, and (Δ) the recently developed 11-interval pulse sequence [28]. All measurements were repeated 3 times and showed a standard deviation of less than 0.002 m/s. Measurements were compared with the expected velocity, given by the dotted black line and calculated as U/ε, where ε is the void fraction. The superficial velocity U was calculated from gas flow meter measurements. Uncertainty for the expected gas velocity, as given by the horizontal error bars, arises from the uncertainty in the void fraction measurement. Parameters for the measurements are shown in Table III.

were used for different calculations in the simulations. The particle diameter used for calculations related to contact mechanics and the weight of the particles was $d_{p,c} = 1.07$ mm, to match the experimental particles. Since spherical particles pack more densely than the experimental particles, the particle diameter used for calculating the void fraction in all aspects of the simulations was reduced to $d_{p,v} = 1.00$ mm so that the void fraction at minimum fluidization from the simulations matched that measured experimentally. The particle diameter used for calculating drag force was increased to $d_{p,d} = 1.55$ mm, so the minimum fluidization velocity given by simulations equaled that measured experimentally. This increase in particle diameter for calculating drag is consistent with nonspherical particles having a larger surface area per unit volume than their spherical counterparts.

Computational fluid dynamics–discrete element method simulations were run for 5 s of simulation time and predictions from times $t = 2$ s to $t = 5$ s were used to generate the maps and probability distribution functions in the next section. The simulations were run on 16 separate 2.3-GHz Intel Xeon E5-2470 processors and each simulation took approximately 30 h to run.

III. RESULTS AND DISCUSSION

For detailed viewing and future comparison of the data presented in this paper, the data is attached as Supplemental Material [44], along with a MATLAB script which reproduces the figures from the data.

TABLE IX. Comparison of average velocity measurements from velocity maps and velocity distributions with expected velocities for packed bed conditions ($U < U_{mf}$).

Measurement	Superficial velocity U (m/s)	Average velocity from MRI (m/s)	Expected velocity from flow meter U/ε (m/s)
gas velocity map	0.065 ± 0.001	0.125 ± 0.004	0.127 ± 0.004
gas velocity map	0.080 ± 0.001	0.147 ± 0.004	0.151 ± 0.004
gas velocity distribution	0.065 ± 0.001	0.122 ± 0.004	0.127 ± 0.004
gas velocity distribution	0.080 ± 0.001	0.146 ± 0.004	0.151 ± 0.004

A. Accuracy of measurements

Figure 3 shows measurements of time-averaged and cross-sectionally-averaged velocities of gas through the bed under packed conditions. The 11-interval sequence is shown to enable quantitative measurements of the gas velocity at up to 0.15 m/s, which corresponds to the gas velocity during fluidization in this setup. The 11-interval sequence was able to measure gas velocity quantitatively at significantly higher velocities than the 13-interval sequence of Cotts *et al.* [20], the previous state of the art for measuring fluid velocities in heterogeneous systems.

In order to understand gas dynamics in further depth, spatially resolved measurements and measurements of gas velocity distribution must be conducted. With these added complexities, the accuracy of the measurements could be questioned further. The averaged velocities deduced from time-averaged velocity maps and velocity probability distribution functions for the bed under packed bed conditions, all from MRI measurements, are compared with expected values, given by U/ε, in Table IX. The measurements are all within 0.01 m/s of the expected value from the flow meter with the greatest differences coming from measurements at the highest superficial velocity. It is difficult to quantify the accuracy of the MRI measurements in the bubbling fluidized bed, since the void fraction oscillated in time and only time-averaged measurements were obtained. However, the measurements in the bubbling fluidized bed are expected to be as accurate as those in packed cases, since background gradients arise from tight packing of particles and there are almost no particles in bubbles. Thus, although the gas moves quickly through bubbles, the measurements of gas velocity in bubbles should be more accurate due to the lack of background gradients. As shown in Fig. 9(a), the gas velocity distribution through the emulsion phase during bubbling is nearly identical to that at minimum fluidization, making the accuracy of measurements in the emulsion phase approximately the same as that in the $U = 0.080$ m/s case.

B. Hydrodynamics at different vertical positions

In order to understand hydrodynamics in the bubbling bed, time-averaged maps of void fraction, particle velocity, and gas velocity were measured using MRI. Figure 4 shows time-averaged void fraction maps at different vertical positions in the bed. The images start at a position in Fig. 4(a) 10 mm above the bed and increase in vertical position to 100 mm above the distributor [Fig. 4(e)]. Figures 4(a)–4(e) all show a time-averaged void fraction larger in the center of the bed than near the walls, indicative of bubbles rising along the axis of the bed. At 10 mm above the distributor [Fig. 4(a)], several regions can be seen in the center of the bed where the void fraction is slightly higher than at the extremities of the bed; the regions of higher void fraction are in a central circular region with a diameter approximately half that of the bed. At a position 25 mm above the distributor [Fig. 4(b)], the void fraction is much higher in the center of the bed over a circular area with a diameter approximately one-third that of the bed. At positions 50–100 mm above the distributor [Figs. 4(c)–4(e)], the contrast between the void fraction in the central region and the region near the walls diminishes, with the region of higher void fraction confined within a diameter slightly larger than in the $z = 25$ mm position [Fig. 4(b)].

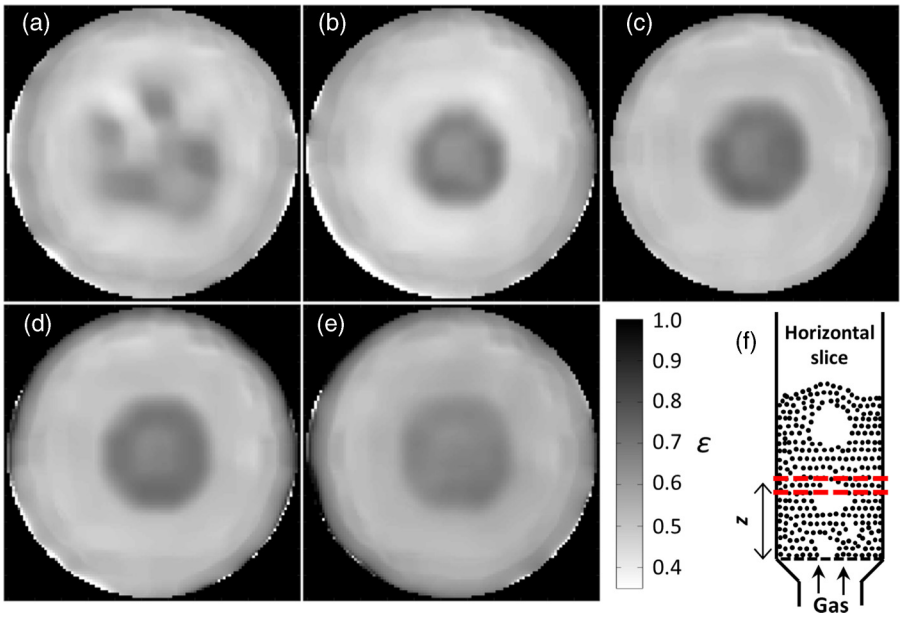

FIG. 4. Time-averaged void fraction maps obtained from intensity maps of poppy seeds at different vertical positions in the fluidized bed. The parameters for the fluidization regime are bubbling; $U = 0.104$ m/s; a field of view $x \times y$ of $53 \times 53\,\text{mm}^2$; a FWHM slice thickness z of 4 mm; a pixel size $x \times y$ of $0.47 \times 0.47\,\text{mm}^2$; vertical positions above the distributor of (a) $z = 10$ mm, (b) $z = 25$ mm, (c) $z = 50$ mm, (d) $z = 75$ mm, and (e) $z = 100$ mm; and an expanded bed height of 120 mm.

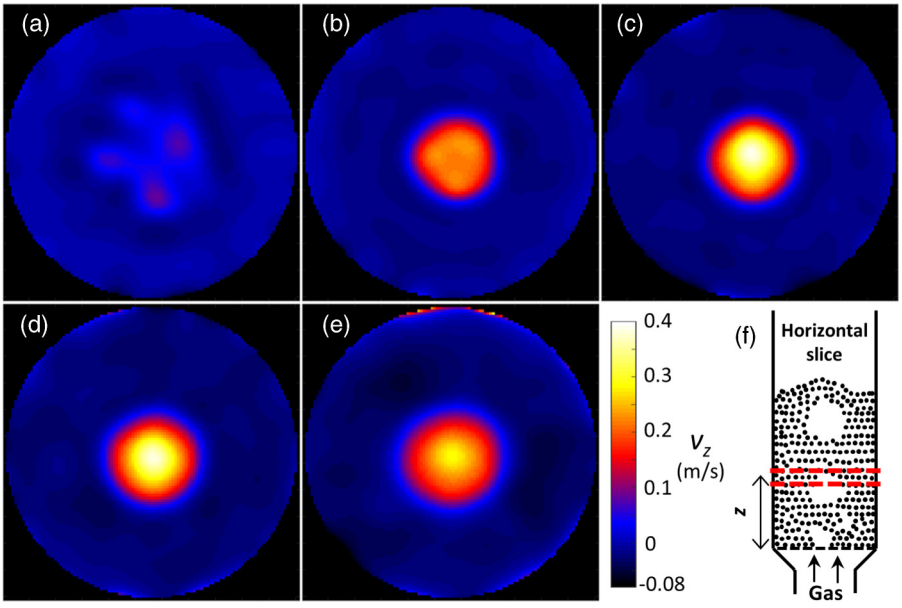

FIG. 5. Time-averaged particle velocity maps of poppy seeds at different vertical positions in the fluidized bed. The parameters for the fluidization regime are bubbling; $U = 0.104$ m/s; a field of view $x \times y$ of $53 \times 53\,\text{mm}^2$; a FWHM slice thickness z of 4 mm; a pixel size $x \times y$ of $0.47 \times 0.47\,\text{mm}^2$; vertical positions above the distributor of (a) $z = 10$ mm, (b) $z = 25$ mm, (c) $z = 50$ mm, (d) $z = 75$ mm, and (e) $z = 100$ mm; and an expanded bed height of 120 mm.

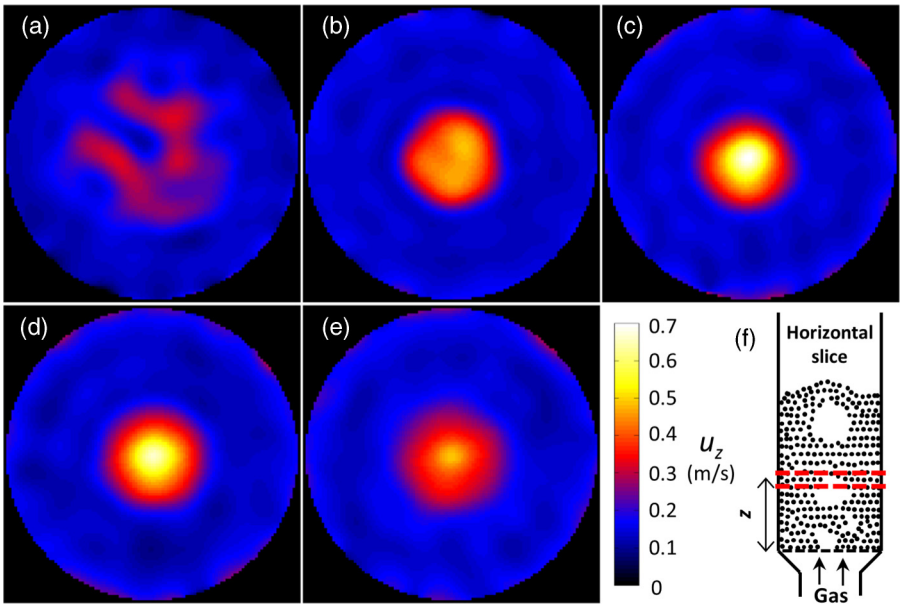

FIG. 6. Maps of time-averaged gas velocity of SF_6 at different vertical positions in the fluidized bed. The parameters for the fluidization regime are bubbling; $U = 0.104$ m/s; a field of view $x \times y$ of 53×53 mm^2; a FWHM slice thickness z of 4 mm; a pixel size $x \times y$ of 0.47×0.47 mm^2; vertical positions above the distributor of (a) $z = 10$ mm, (b) $z = 25$ mm, (c) $z = 50$ mm, (d) $z = 75$ mm, and (e) $z = 100$ mm; and an expanded bed height of 120 mm.

Figure 5 shows maps of the time-averaged vertical particle velocity v_z at different vertical positions in the bed of particles. These maps show an upward moving profile in the center of the bed with time-averaged velocities of up to 0.4 m/s. The diameter of this upward velocity region is similar to the diameter of the high void fraction region for the corresponding void fraction images in Fig. 4. In Figs. 5(b)–5(e) the region of upward velocity is surrounded by a much larger region of downward velocity with an almost uniform time-averaged velocity just below 0 m/s. For the $z = 10$ mm case in Fig. 5(a), the profile is similar to those in Figs. 5(b)–5(e), except that the upward moving profile is slightly wider and the maximum time-averaged velocity is only about 0.1 m/s.

Figure 6 shows time-averaged maps of the vertical component of gas velocity u_z at the same positions and the same fluidizing velocity as Figs. 4 and 5. Qualitatively, the maps look very similar to those for particle velocity at the corresponding vertical position in the bed of particles. For $z = 25$–100 mm above the distributor in Figs. 6(b)–6(e), there is a region of fast upward velocities (up to 0.7 m/s) in the center of the bed and a region of much lower upward velocities (around 0.15 m/s) in the larger outer annulus of pixels. In Fig. 6(a) a wider central profile shows gas velocities up to 0.25 m/s, while the outer annulus has upward gas velocities around 0.1 m/s.

The results for particle and gas velocity, as well as void fraction, at $U = 0.104$ m/s in Figs. 4–6 are consistent with a stream of bubbles rising through the center of the bed. Because bubbles have a void fraction close to unity, having bubbles periodically pass through the center of the bed would lead to a higher time-averaged void fraction in the center of the bed than near the walls, as seen in Figs. 4(b)–4(e). Bubbles often form after very small void regions coalesce just above the distributor, explaining the wide region of higher time-averaged void fraction seen 10 mm above the distributor in Fig. 4(a). In bubbling fluidized beds, it is common to see a Gulf-Stream–like pattern in which particles move quickly upward in the wakes of bubbles and then slowly downward near the walls. This pattern is consistent with the time-averaged particle velocities seen in Fig. 5. The gas flow in a fluidized bed is usually greatest through the bubbles as there is less resistance to flow due to the

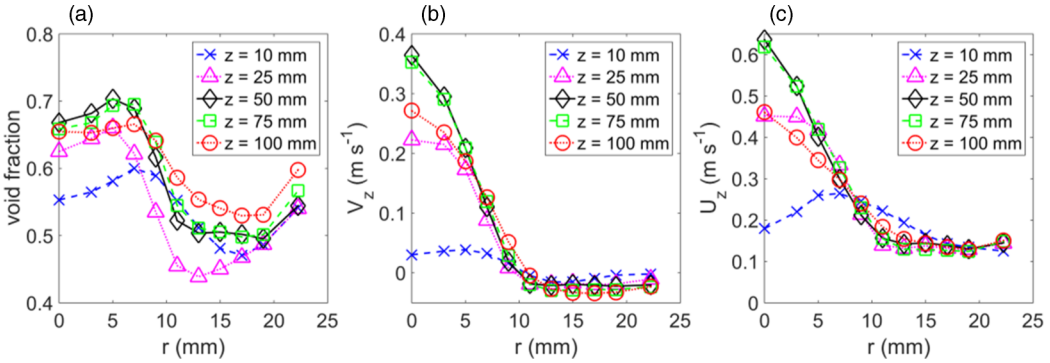

FIG. 7. MRI measurements of time-averaged (a) void fraction, (b) vertical particle velocity and (c) vertical gas velocity as a function of radial position at different heights z above the distributor, with an expanded bed height of 120 mm.

small numbers of particles in the bubbles. This flow pattern is consistent with the time-averaged gas velocities seen in Fig. 6.

An alternative explanation for the gas and particle motion seen in Figs. 4–6 would be the formation of a jet or spout. This explanation seems, at first, plausible, since the sizes of the time-averaged void regions are fairly narrow and do not change much with distance above the distributor in the $z = 25$–100 mm range. However, it is unlikely that a spout would have formed because a porous distributor with a significant pressure drop was used; this would give an even distribution of gas, rather than a jet. Additionally, if a jet were formed, the maximum gas and particle velocities would be expected at the $z = 10$ mm position. Experimentally, the gas and particle velocities in the center of the bed increased to a maximum between 50 and 75 mm above the distributor, consistent with the velocity arising from the motion of bubbles.

The results at $z = 10$ mm are particularly interesting because they are most different from the results at other heights in the bed and they demonstrate the least azimuthal symmetry. As discussed earlier, we explain the behavior seen at $z = 10$ mm as a position at which smaller bubbles are forming before they quickly coalesce into a single central bubble before the $z = 25$ mm height. From the void fraction map in Fig. 4(a) there appear to be four or five small regions with higher void fraction near the center of the bed, but not arranged in a radially symmetric manner. The velocity maps in Figs. 5(a) and 6(a) are indicative of particles and gas rising faster in these four or five regions. This pattern can be explained by defects in the distributor or instabilities in the flow causing persistent nucleation points for bubbles just below these four or five regions. Since the averaging time for these experiments was such that thousands of bubbles were able to form over the course of the averaging, it seems likely that these are indeed persistent flow features and unlikely that a different or more radially symmetric pattern would form at $z = 10$ mm if a larger averaging time were used.

To compare flow behavior at different heights in the bed more quantitatively, Fig. 7 shows line plots for the void fraction [Fig. 7(a)], particle velocity [Fig. 7(b)], and gas velocity [Fig. 7(c)] as a function of radial position for different heights in the bed. Similar flow patterns can be seen at $z = 25$–100 mm, with a higher void fraction and velocities in the center of the bed due to bubbles rising through this central region. The similarity of these line plots is indicative that bubbles maintain a similar size without coalescing or splitting within this range of heights. The void fraction surprisingly increases close to the walls in this region; this is likely due to particles not being able to pack as closely near the walls as well as artifacts due to inhomogeneity in the magnetic field near the walls. The void fraction is slightly lower in the very center of the bed than at radial positions $r \sim 2$–8 mm. As shown in Fig. 8(h), the same trend is seen in CFD-DEM simulations. Computational fluid dynamics–discrete element method simulations show that this void fraction pattern arises due

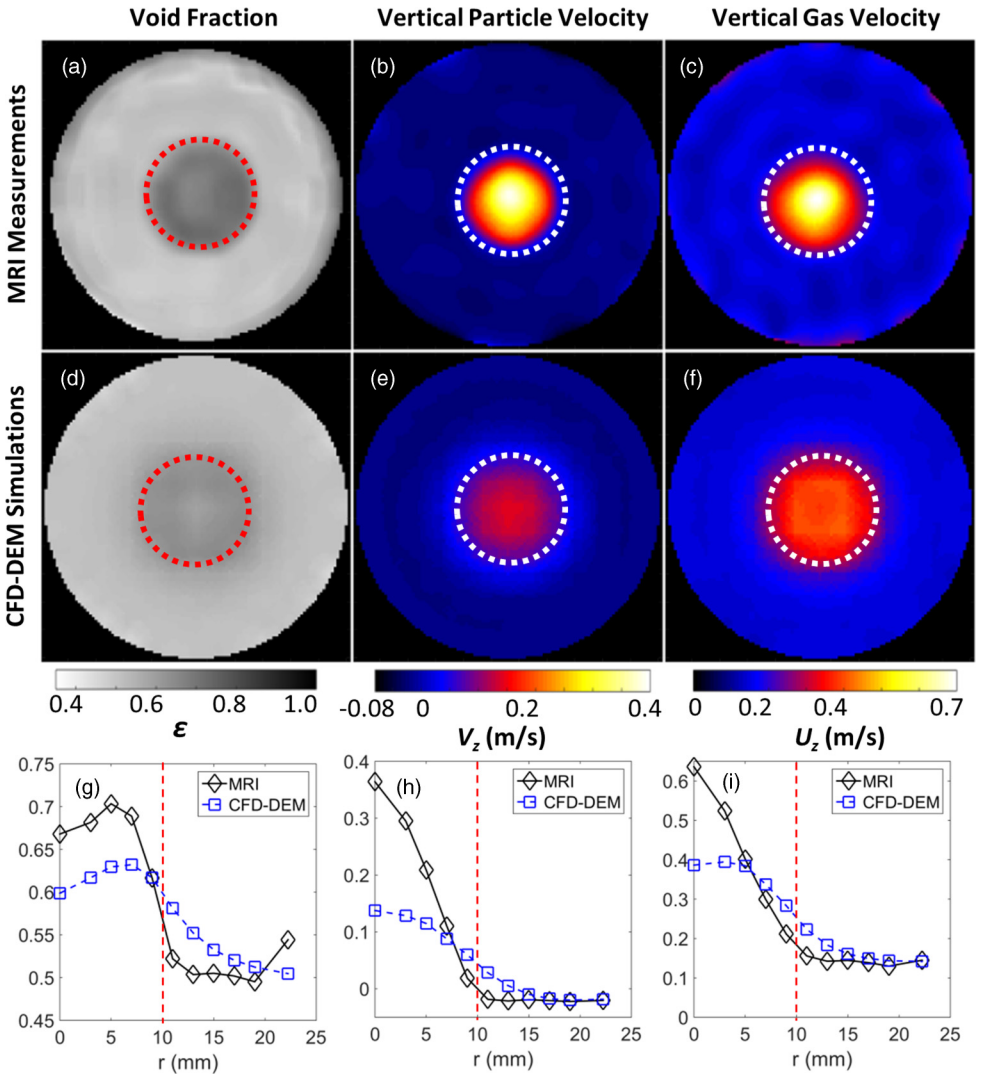

FIG. 8. (a)–(f) Comparison of cross-sectional maps of the time-averaged void fraction (first column), vertical particle velocity (second column), and vertical gas velocity (third column) for (a)–(c) MRI measurements and (d)–(f) CFD-DEM simulations. (g)–(i) Line plots for the void fraction and particle and gas velocities versus radial position. The bubbling region is (a)–(f) inside the dotted lines and (g)–(i) to the left of the vertical dotted line. The emulsion region is (a)–(f) outside the dotted lines and (g)–(i) to the right of the dotted lines. The field of view $x \times y$ is $53 \times 53\,\mathrm{mm}^2$, the slice thickness z is 4 mm, and the pixel size $x \times y$ is $0.47 \times 0.47\,\mathrm{mm}^2$. The height above the distributor was $z = 50$ mm.

to bubbles having a dimple at their bottom, thus creating slightly more void region at $r \sim 5$ mm than $r \sim 0$ mm. In the $z = 25$–100 mm range, nearly identical hydrodynamics are observed for the $z = 50$ and 75 mm heights, while profiles with slightly lower void fractions and velocities in the center of the bed are observed for the $z = 25$ and 100 mm heights. The lower velocities and void fractions at $z = 25$ mm are likely indicative that the bubbles are still growing and developing into a stable state at this height. The lower values at $z = 100$ mm are likely indicative of deformation of the bubbles as they approach the bed surface, given the fact that the bubbles are approximately 20 mm in diameter and the expanded bed height is approximately 120 mm. These same trends were

TABLE X. Average values of void fraction and velocities from MRI maps in Figs. 8(a)–8(c), CFD-DEM maps in Figs. 8(d)–8(f), and as predicted by two-phase theory [9,45].

Region of bed	Average void fraction ε_{avg}	Average particle velocity (m/s)	Average gas velocity (m/s)
emulsion region (MRI)	0.51 ± 0.02	-0.021 ± 0.004	0.147 ± 0.004
emulsion region (CFD-DEM)	0.52	–0.01	0.15
emulsion region (two-phase theory)	0.51 ± 0.02		0.155 ± 0.006
bubbling region (MRI)	0.66 ± 0.02	0.130 ± 0.004	0.340 ± 0.004
bubbling region (CFD-DEM)	0.63	0.10	0.35

seen in CFD-DEM simulations due to bubble growth low in the bed and bubble deformation high in the bed. The nearly identical profiles for $z = 50$ and 75 mm are likely indicative that the bubbles are fully developed in this range of heights and are not influenced by entrance or exit effects. For $z = 10$ mm, the same trends are seen as at the other heights, but the maximum void fraction and velocity reached are much lower than at higher points in the bed; this is likely due to small bubbles forming and coalescing at this height before fully formed bubbles persist higher in the bed.

C. Comparison with computational and analytical models

In order to shed light on the accuracy of computational and analytical models, predictions from these models were compared with MRI measurements. Figure 8 shows time-averaged maps of the void fraction and vertical velocities of both particles and gas measured using MRI at a height $z = 50$ mm above the gas distributor at the base of the bed. The superficial velocity of the gas was 0.104 m/s. In Fig. 8(a) a central region, approximately 20 mm in diameter, can be seen with a void fraction significantly higher than that outside the dotted lines. The void fraction distribution shown in Fig 8(a) is indicative of a stream of bubbles passing successively through the central region of the bed, as demonstrated in Figs. 4–6. Beyond a radius of 10 mm, the void fraction is ~0.51, equal to the void fraction at minimum fluidization. Thus, few bubbles, if any, pass through the outer region of the bed. For ease of reference, the regions inside and outside the dotted lines of Fig. 8(a) are referred to here as the bubbling region and the emulsion region, respectively. Figures 8(b) and 8(c) show that particle and gas velocities are significantly higher in the bubbling region than in the emulsion region, consistent with classical theory [6]. The reasoning for the cutoff line being at $r = 10$ mm and the sensitivity of results to this selection are discussed in the Appendix.

In a fluidized bed reactor, the gas velocities in the bubble and emulsion phases determine the contacting of gaseous reactants with reacting solids [6]. Classical theory postulates that for bubbling fluidization, the gas velocity relative to the particles [45] and the void fraction in the emulsion phase are both equal to those at minimum fluidization, U_{mf}/ε_{mf} and ε_{mf}, respectively [9]. Thus, the gas velocity in the emulsion phase $u_{z,e}$ is given by

$$u_{z,e} = U_{mf}/\varepsilon_{mf} + v_{z,e}, \tag{8}$$

where $v_{z,e}$ is the vertical component of the average particle velocity in the emulsion phase. However, there has been significant debate over the correct division of gas flow between bubbles and interstitial flow [46–48]. Table X indicates that classical theory is in excellent agreement with MRI measurements of the average void fraction and gas velocity in the emulsion phase for this particular system.

The design of fluidized beds for new applications is facilitated by the use of computational models, which require experimental validation [12]. To date such studies have been restricted to experimental measurements of particle motion and void fraction [49,50]; however, the greatest uncertainty in some of these models has been attributed to the interaction of the gas and solids [51]. Figures 8(d)–8(f) show predictions from CFD-DEM simulations [52] of time-averaged hydrodynamics in the bubbling

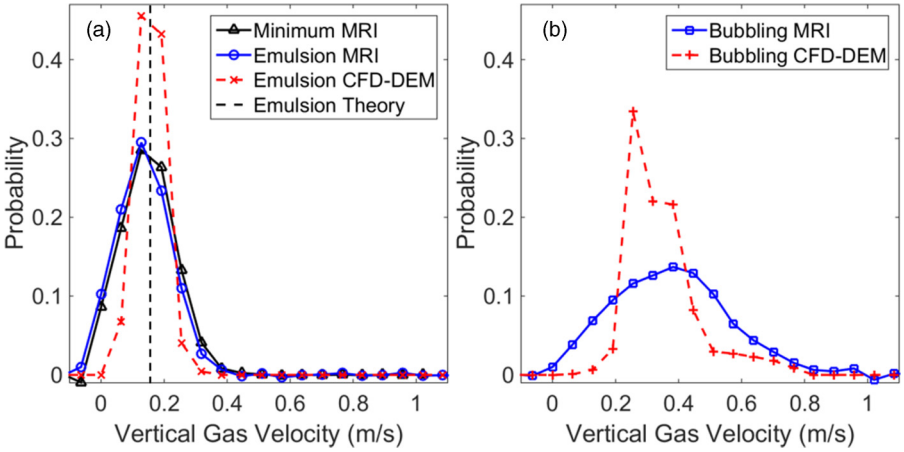

FIG. 9. Probability distribution functions of vertical gas velocity in (a) the emulsion region and (b) the bubbling region (regions shown in Fig. 8). MRI measurements were compared with CFD-DEM predictions. In (a), a comparison is also given with MRI measurement of velocity distribution across the entire cross section at minimum fluidization and the vertical dashed line gives the prediction of analytical theory (8) [9,45] for gas velocity in the emulsion region.

bed for direct comparison with MRI measurements in Figs. 8(a)–8(c). The CFD-DEM simulates the motion of each individual particle, according to Newtonian and contact mechanics, while simulating gas motion on a CFD grid and coupling the phases using a drag law. These simulations are at too small a scale to be used in the design of industrial reactors directly; however, they form a key part of the multiscale simulation methodology that is required to develop simulations of industrial scale processes [10,42]. Here effective particle diameters were used in calculations of drag and void fraction in the simulations in order to model the nonsphericity of the poppy seeds. The maps produced from CFD-DEM simulations in Figs. 8(d)–8(f) show patterns consistent with MRI results, shown in Figs. 8(a)–8(c). Figures 8(g)–8(i) shows that the simulations capture the features of the experimental data, but produce lower values for the gas void fraction and velocity in the center of the bed. Table X shows that predictions from the simulation for the emulsion and bubbling regions match the experimental results very closely when averaging over the regions, with the largest difference being in the particle velocity in the bubbling region. The agreement between the MRI measurements and CFD-DEM predictions indicates that nonsphericity can be adequately modeled by incorporating effective particle diameters to match the values of U_{mf} and ε_{mf} seen experimentally for nonspherical particles.

Additional MRI measurements were conducted to obtain the full probability distribution function of vertical gas velocities, as shown in Fig. 9. Interstitial velocities ranging from approximately 0 to 0.4 m/s can be seen in the emulsion region, with a distribution close to Gaussian [Fig. 9(a)]. The particle Reynolds number ($\mathrm{Re} = \rho U d_p/\mu$) is ~400 for this system, indicating flow in the transitional regime to turbulent flow. Higher gas velocities, ranging from approximately 0 to 1.0 m/s, were measured in the bubbling region with a distribution skewed slightly towards lower velocities [Fig. 9(b)]. Figure 9(a) shows that the measured distribution in the emulsion region (labeled Emulsion MRI) is nearly identical to that measured at minimum fluidization (labeled Minimum MRI), but is shifted to lower gas velocities by about 0.02 m/s to account for the average downward motion of the particulate phase as noted above. Two-phase theory postulates that the mean gas velocity through the emulsion phase is similar to that at minimum fluidization [9]; our measurements reveal a stronger result, namely, that the full velocity distribution is very similar.

The distributions predicted by CFD-DEM simulations (Fig. 9) are similar in shape and modal velocity to the MRI results, but the standard deviation of the distribution measured experimentally

in the emulsion region is 2.2 times greater than that given by the simulations. We attribute this difference in width to the fact that MRI measurements capture the full distribution of velocities, accounting for each gas molecule, while CFD-DEM is inherently limited to predicting only the average gas velocity in fluid cells larger than the particle diameter. In practice, a no-slip boundary condition must exist between the gas and the surface of each particle, necessitating appreciable gas velocity variations in every void space between particles; neither this nor turbulence is accounted for in CFD-DEM simulations.

The velocity distribution affects interphase species and energy transfer, thus capturing the distribution accurately is necessary for accurate modeling of many reactors. Models are available to describe distributions of velocities arising from free fluid turbulence at a subgrid scale [18], but these are unlikely to be applicable here as the variations in velocity are induced by flow around the particles and the particle concentration is very high. Analytical and computational models, similar to turbulence models but accounting for the influence of many particles on flow, need to be developed to account for the effects of these particle-scale distributions of velocities on transport and ultimately on chemical reactions.

IV. CONCLUSION

In this paper MRI measurements were introduced to shed light on coupled gas-solid flow, using a bubbling fluidized bed as an example. Quantitative measurements of the gas and particle velocity were presented, as well as measurements of the local void fraction within the bed. Measurements show that the mean velocity is consistent with classical analytical theory, but that a wide distribution of velocities exists. These techniques will be useful to probe flows in more complex and inadequately characterized systems, such as fluidized and moving beds involving a third liquid phase, interparticle forces, rapid phase changes, or temperature gradients from exothermic reactions.

ACKNOWLEDGMENTS

C.M.B. acknowledges financial support from the Gates Cambridge Trust and Syncrude Canada Ltd. C.M.B. also acknowledges Meenal Pore, Christine Schmaus, Nicholas Ramskill, and Mick Mantle for help with the experimental setup.

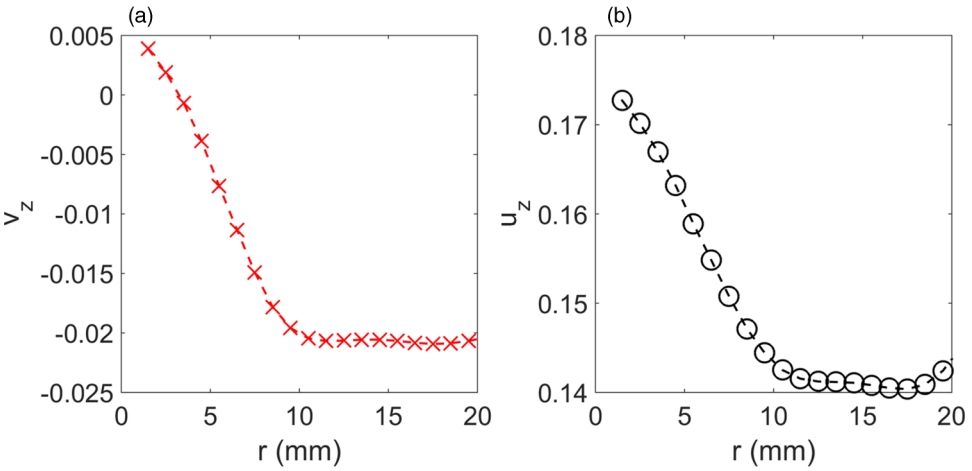

FIG. 10. (a) Particle velocity and (b) gas velocity in the emulsion region for the experimental data as a function of the radius used for the cutoff between the bubbling and emulsion regions.

APPENDIX: DIVIDING POINT BETWEEN EMULSION AND BUBBLING REGIONS

As shown in Fig. 8, the lines dividing the bubbling and emulsion regions were drawn at a value $r = 10$ mm. These lines were drawn based on a point of a large gradient in the void fraction, very close to where the void fraction becomes essentially constant with increasing radial position for the experimental data. This can be seen in Fig. 8(h). Additionally, the particle and gas velocities also reached a near constant value with increasing radius at the dividing line between the bubbling and emulsion regions. The same dividing lines were used for the experimental and computational model data. For the experimental data, the results were more sensitive to the dividing line than for the computational data because there was a more sharp division between the bubbling and emulsion regions, based on gradient in void fraction, for the experimental data. Figure 10 shows the sensitivity of particle velocity and gas velocity in the emulsion region as a function of the dividing line. If the radius of the bubbling region were significantly smaller than 10 mm, a different value would be recorded; however, if the value were increased a nearly identical value would be recorded, indicating that a radius of 10 mm is the point at which the emulsion region starts.

[1] R. M. Iverson, The physics of debris flows, Rev. Geophys. **35**, 245 (1997).
[2] X. Cheng, J. H. McCoy, J. N. Israelachvili, and I. Cohen, Imaging the microscopic structure of shear thinning and thickening colloidal suspensions, Science **333**, 1276 (2011).
[3] H. M. Jaeger, S. R. Nagel, and R. P. Behringer, Granular solids, liquids and gases, Rev. Mod. Phys. **68**, 1259 (1996).
[4] R. D. Maladen, Y. Ding, C. Li, and D. I. Goldman, Undulatory swimming in sand: Subsurface locomotion of the sandfish lizard, Science **325**, 314 (2009).
[5] H. K. Pak and P. R. Behringer, Bubbling in vertically vibrated granular materials, Nature (London) **371**, 231 (1994).
[6] J. F. Davidson and D. Harrison, *Fluidised Particles* (Cambridge University Press, Cambridge, 1963).
[7] J. R. Royer, D. J. Evans, L. Oyarte, Q. Guo, E. Kapit, M. E. Möbius, S. R. Waitukaitis, and H. M. Jaeger, High-speed tracking of rupture and clustering in freely falling granular streams, Nature (London) **459**, 1110 (2009).
[8] T. A. Bell, Challenges in the scale-up of particulate processes—An industrial perspective, Powder Technol. **150**, 60 (2005).
[9] R. D. Toomey and H. F. Johnstone, Gaseous fluidization of solid particles, Chem. Eng. Prog. **48**, 220 (1952).
[10] M. A. van der Hoef, M. van Sint Annaland, N. G. Deen, and J. A. M. Kuipers, Numerical simulation of dense gas-solid fluidized beds: A multiscale modeling strategy, Annu. Rev. Fluid Mech. **40**, 47 (2008).
[11] R. M. Contractor, D. I. Garnett, H. S. Horowitz, H. E. Bergna, G. S. Patience, J. T. Schwartz, and G. M. Sisler, *Proceedings of the Second World Congress and Fourth European Workshop Meeting* (Elsevier, Amsterdam, 1994).
[12] M. P. Dudukovic, Frontiers in reactor engineering, Science **325**, 698 (2009).
[13] E. E. Ehrichs, H. M. Jaeger, G. S. Karczmar, J. B. Knight, V. Y. Kuperman, and S. R. Nagel, Granular convection observed by magnetic resonance imaging, Science **267**, 1632 (1995).
[14] C. R. Müller, D. J. Holland, A. J. Sederman, M. D. Mantle, L. F. Gladden, and J. F. Davidson, Magnetic resonance imaging of fluidized beds, Powder Technol. **183**, 53 (2008).
[15] V. Verma, J. T. Padding, N. G. Deen, J. A. M. H. Kuipers, F. Barthel, M. Bieberle, M. Wagner, and U. Hampel, Bubble dynamics in a 3-D gas—Solid fluidized bed using ultrafast electron beam x-ray tomography and two-fluid model, AIChE J. **60**, 1632 (2014).
[16] P. T. Callaghan, A. Coy, D. MacGowan, K. J. Packer, and F. O. Zelaya, Diffraction-like effects in NMR diffusion studies of fluids in porous solids, Nature (London) **351**, 467 (1991).
[17] S. S. Datta, H. Chiang, T. S. Ramakrishnan, and D. A. Weitz, Spatial Fluctuations of Fluid Velocities in Flow Through a Three-Dimensional Porous Medium, Phys. Rev. Lett. **111**, 064501 (2013).

[18] S. Balachandar and J. K. Eaton, Turbulent dispersed multiphase flow, Annu. Rev. Fluid Mech. **42**, 111 (2010).
[19] M. H. Sankey, D. J. Holland, L. F. Gladden, and A. J. Sederman, Magnetic resonance velocity imaging of liquid and gas two-phase flow in packed beds, J. Magn. Reson. **196**, 142 (2009).
[20] R. M. Cotts, M. J. R. Hoch, T. Sun, and J. T. Markert, Pulsed field gradient stimulated echo methods for improved NMR diffusion measurements in heterogeneous systems, J. Magn. Reson. 1969. **83**, 252 (1989).
[21] N. Spindler, P. Galvosas, A. Pohlmeier, and H. Vereecken, NMR velocimetry with 13-interval stimulated echo multi-slice imaging in natural porous media under low flow rates, J. Magn. Reson. **212**, 216 (2011).
[22] N. M. Homan, B. Venne, and H. Van As, Flow characteristics and exchange in complex biological systems as observed by pulsed-field-gradient magnetic-resonance imaging, Phys. Rev. E **82**, 026310 (2010).
[23] R. Wang, M. S. Rosen, D. Candela, R. W. Mair, and R. L. Walsworth, Study of gas-fluidization dynamics with laser-polarized 129Xe, Magn. Reson. Imaging **23**, 203 (2005).
[24] D. Candela, C. Huan, K. Facto, R. Wang, R. W. Mair, and R. L. Walsworth, NMR measurements of grain and gas motion in a gas-fluidized granular bed, Granul. Matter. **9**, 331 (2007).
[25] T. Pavlin, R. Wang, R. McGorty, M. S. Rosen, D. G. Cory, D. Candela, R. W. Mair, and R. L. Walsworth, Noninvasive measurements of gas exchange in a three-dimensional fluidized bed by hyperpolarized 129Xe NMR, Appl. Magn. Reson. **32**, 93 (2007).
[26] R. W. Mair, M. S. Rosen, R. L. Walsworth, R. Wang, D. G. Cory, and D. Candela, NMR studies of laser-polarized xenon gas flow in porous and granular media, available at http://adsabs.harvard.edu/abs/2003APS..DMP.J1126M
[27] D. Geldart, Types of fluidization, Powder Technol. **7**, 285 (1973).
[28] C. M. Boyce, N. P. Rice, A. J. Sederman, J. S. Dennis, and D. J. Holland, 11-interval PFG pulse sequence for improved measurement of fast velocities of fluids with high diffusivity in systems with short T_2^*, J. Magn. Reson. **265**, 67 (2016).
[29] A. Jerschow and R. Kumar, Calculation of coherence pathway selection and cogwheel cycles, J. Magn. Reson. **160**, 59 (2003).
[30] E. Hahn, Spin echoes, Phys. Rev. **80**, 580 (1950).
[31] M. Lustig, D. L. Donoho, and J. M. Pauly, Sparse MRI: The application of compressed sensing for rapid MR imaging, Magn. Reson. Med. **58**, 1182 (2007).
[32] C. Goniva, C. Kloss, N. G. Deen, J. A. M. Kuipers, and S. Pirker, Influence of rolling friction on single spout fluidized bed simulation, Particuology **10**, 582 (2012).
[33] C. Kloss, C. Goniva, A. Hager, S. Amberger, and S. Pirker, Models, algorithms and validation for opensource DEM and CFD–DEM, Prog. Comput. Fluid Dyn. Int. J. **12**, 140 (2012).
[34] H. G. Weller, G. Tabor, H. Jasak, and C. Fureby, A tensorial approach to computational continuum mechanics using object-oriented techniques, Comput. Phys. **12**, 620 (1998).
[35] C. M. Boyce, D. J. Holland, S. A. Scott, and J. S. Dennis, Limitations on fluid grid sizing for using volume-averaged fluid equations in discrete element models of fluidized beds, Ind. Eng. Chem. Res. **54**, 10684 (2015).
[36] C. M. Boyce, D. J. Holland, S. A. Scott, and J. S. Dennis, Novel fluid grid and voidage calculation techniques for a discrete element model of a 3D cylindrical fluidized bed, Comput. Chem. Eng. **65**, 18 (2014).
[37] C. M. Boyce, J. F. Davidson, D. J. Holland, S. A. Scott, and J. S. Dennis, The origin of pressure oscillations in slugging fluidized beds: Comparison of experimental results from magnetic resonance imaging with a discrete element model, Chem. Eng. Sci. **116**, 611 (2014).
[38] C. M. Boyce, D. J. Holland, S. A. Scott, and J. S. Dennis, Adapting data processing to compare model and experiment accurately: A discrete element model and magnetic resonance measurements of a 3D cylindrical fluidized bed, Ind. Eng. Chem. Res. **52**, 18085 (2013).
[39] C. R. Müller, D. J. Holland, A. J. Sederman, S. A. Scott, J. S. Dennis, and L. F. Gladden, Granular temperature: Comparison of magnetic resonance measurements with discrete element model simulations, Powder Technol. **184**, 241 (2008).

[40] Y. F. Sharobeem, Apparent dynamic friction coefficients for grain crops, Misr J. Agric. Eng. **24**, 557 (2007).
[41] T. B. Anderson and R. Jackson, Fluid mechanical description of fluidized beds. Equations of motion, Ind. Eng. Chem. Fundam. **6**, 527 (1967).
[42] S. Radl and S. Sundaresan, A drag model for filtered Euler-Lagrange simulations of clustered gas-particle suspensions, Chem. Eng. Sci. **117**, 416 (2014).
[43] R. Beetstra, M. A. Van Der Hoef, and J. A. M. Kuipers, Drag force of intermediate Reynolds number flow past mono- and bidisperse arrays of spheres, AIChE J. **53**, 489 (2007).
[44] See Supplemental Material at http://link.aps.org/supplemental/10.1103/PhysRevFluids.1.074201 for MATLAB files.
[45] J. F. Davidson and D. Harrison, The behaviour of a continuously bubbling fluidised bed, Chem. Eng. Sci. **21**, 731 (1966).
[46] J. R. Grace and R. Clift, On the two-phase theory of fluidization, Chem. Eng. Sci. **29**, 327 (1974).
[47] C. Yacono, P. N. Rowe, and H. Angelino, An analysis of the distribution of flow between phases in a gas fluidised bed, Chem. Eng. Sci. **34**, 789 (1979).
[48] J. Werther and E. Hartge, Modeling of industrial fluidized-bed reactors, Ind. Eng. Chem. Res. **43**, 5593 (2004).
[49] C. R. Müller, S. A. Scott, D. J. Holland, B. C. Clarke, A. J. Sederman, J. S. Dennis, and L. F. Gladden, Validation of a discrete element model using magnetic resonance measurements, Particuology. **7**, 297 (2009).
[50] J. Link, C. Zeilstra, N. G. Deen, and J. A. M. Kuipers, Validation of a discrete particle model in a 2D spout-fluid bed using non-intrusive optical measuring techniques, Can. J. Chem. Eng. **82**, 30 (2004).
[51] S. H. L. Kriebitzsch, M. A. Van Der Hoef, and J. A. M. Kuipers, Drag force in discrete particle models—Continuum scale or single particle scale? AIChE J. **59**, 316 (2013).
[52] Y. Tsuji, T. Kawaguchi, and T. Tanaka, Discrete particle simulation of two-dimensional fluidized bed, Powder Technol. **77**, 79 (1993).